Nano Research

Open Access

Research Article

Photochemically fabricated peptide hydrogels from de novo design to application in antibacterial therapy and wound healing

Xiang Shu[1,§], Zhaoyang Wang[1,§], Ying Wen[1], Yuexin Shi[1], Xue-Wang Gao[2,3], Shumin Yang[1], Jianqun Shao[1], Ke Feng[2,3], Bin Chen[2,3], Nan Xie[1] ✉, Chen-Ho Tung[2,3], and Li-Zhu Wu[2,3] ✉

[1] *School of Pharmaceutical Sciences, Capital Medical University, Beijing 100069, China*
[2] *Key Laboratory of Photochemical Conversion and Optoelectronic Materials & CAS-HKU Joint Laboratory on New Materials, New Cornerstone Science Laboratory, Technical Institute of Physics and Chemistry, The Chinese Academy of Sciences, Beijing 100190, China*
[3] *School of Future Technology, University of Chinese Academy of Sciences, Beijing 100049, China*
§ *Xiang Shu and Zhaoyang Wang contributed equally to this work.*

Cite this article: *Nano Research*, **2026**, *19*, 94908544. https://doi.org/10.26599/NR.2026.94908544

ABSTRACT: De novo designed peptide amphiphiles have been exemplified as building blocks for direct fabrication of biofunctional hydrogels through a photochemical approach. Herein, by incorporating diphenylalanine (FF) as a self-assembling antibacterial motif and dityrosine (YY) as a photocrosslinkable unit, the peptide sequences are interconnected through alternating hydrophilic D (*L*-aspartate) and hydrophobic X (*ε*-aminocaproic acid) residues to achieve a precise balance between non-covalent fibrillization and covalent crosslinking. Upon visible-light irradiation, these peptides undergo rapid photocrosslinking in aqueous media, yielding hydrogels with tunable gelation properties, robust mechanical stability, and adjustable functionality. The optimized 4Y6F hydrogel exhibits strong antibacterial efficacy against both Gram-positive and Gram-negative bacteria, attributed to synergistic structural interactions. *In vivo* wound healing studies demonstrate accelerated re-epithelialization, enhanced collagen deposition, and improved angiogenesis, significantly outperforming control groups and commercial formulations. This study presents a versatile peptide platform for the photochemical fabrication of hydrogels, advancing from de novo design to practical applications in antibacterial therapy and wound healing, and offering a promising bottom-up approach for a wide range of biomedical scenarios.

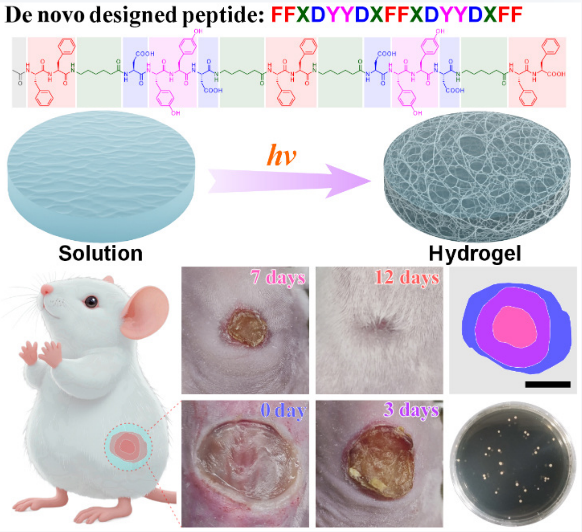

KEYWORDS: peptide hydrogels, de novo design, photocrosslinking, antibacterial activity, wound healing

1 Introduction

Peptides, widely recognized as versatile building blocks for soft materials [1–6], provide a bottom-up route for direct hydrogel fabrication owing to their routine synthesis, sequence encodability, and intrinsic biocompatibility [7–17]. Conventionally, peptide hydrogels form through noncovalent interactions, including hydrogen bonding [18–21], hydrophobic and hydrophilic interactions [22–24], van der Waals forces [25–27], ionic interactions [28–32], and π-π stacking [33–36], which drive spontaneous self-assembly into well-defined structures such as ribbons [37–39], rods [40–42], sheets [43–46], and tubes [47–50] that subsequently percolate into 3D networks. However, purely noncovalent peptide hydrogels are inherently metastable, making them highly sensitive to changes in pH, temperature, ionic strength, dilution, and mechanical perturbation. To enhance stability, covalent crosslinking is often superimposed on peptide assemblies to lock in the desired supramolecular organization [51, 52]. Representative strategies include oxidative formation of disulfide crosslinks [53, 54], polymerization of terminal alkenes [55–59], thiol-ene reactions, enzyme-mediated couplings [60, 61], and metal-

Received: December 2, 2025; **Revised:** February 5, 2026
Accepted: February 6, 2026

✉Address correspondence to Nan Xie, nanxie@ccmu.edu.cn; Li-Zhu Wu, lzwu@mail.ipc.ac.cn

ligand coordination [62, 63]. Nevertheless, integrating multiple orthogonal functions within a single peptide strand remains challenging.

Precise sequence encoding defines charge distribution, amphiphilicity, and reactive-residue placement, promoting fibrillization and enabling biofunctional innovation [2, 49]. From a design perspective, multifunctional peptide hydrogels rely on the rational integration of self assembly motifs, stimuli responsive crosslinkable units, and sequence level control of hydrophobic and hydrophilic balance, allowing coordinated control of mechanical performance and biological function. Drawing on our experience, de novo sequence design enables multifunctional peptide platforms in which light-responsive dityrosine (YY) motifs afford photochemical crosslinking [64, 65]. Such crosslinking can be introduced with spatiotemporal control while preserving hydrophilic-hydrophobic balance, ionic complementarity, and π-π stacking, thereby supporting the emergence of higher-order hierarchical architectures. Within this scaffold, sequence-encodable peptides could serve as programmable building blocks for direct hydrogel fabrication at the molecular level.

Building on above attributes, this research aims to employ a one-pot photochemical strategy to fabricate functional hydrogels directly from de novo designed peptide strands for representative biomedical applications, exemplified by antibacterial therapy and wound healing. The de novo designed peptide sequences are tailored with their structure incorporating four essential components: (1) hydrophobic diphenylalanine (FF) motif that imparts antibacterial activity, drives self-assembly through aromatic interactions, and stabilizes fibrillar networks; (2) photo-crosslinkable YY motif enabling rapid and efficient hydrogel formation under visible-light irradiation; (3) pentamethylene-based hydrophobic spacer (X) that modulates the spacing between YY and FF modules, increases molecular flexibility, and creates controlled structural intervals; (4) alternating charged L-aspartate (D) and hydrophobic X residues engineered to balance molecular amphiphilicity, enhance hydrophilicity, and regulate charge distribution. Systematic variation of these sequence modules allows structure-activity relationships to be established between peptide composition, supramolecular assembly, crosslinking behavior, and hydrogel performance. This comprehensive design is expected to enable the creation of peptide hydrogels with customized antibacterial activity, optimized mechanical properties, and well-defined hierarchical structures, advancing their potential in wound healing and broader biomedical applications.

2 Experimental

2.1 De novo designed peptide synthesis

All peptides were synthesized using the standard 9-fluorenylmethoxycarbonyl (Fmoc) solid-phase peptide synthesis (SPPS) method on 2-chlorotrityl chloride (CTC) resin. Each amino acid coupling was performed with 3 equivalents of *o*-benzotriazole-*N*,*N*,*N*',*N*'-tetramethyluroniumhexafluorophosph-ate/*N*-hydroxybenzotriazole (HBTU/HOBt). The N-terminal protecting groups were removed by treating with a 20/80 (v/v) solution of piperidine/*N*,*N*-dimethylformamide (DMF). Upon completion of the SPPS, the peptides were cleaved from the resin using a mixture of trifluoroacetic acid/triisopropylsilane/H_2O (TFA/TIPS/H_2O, 95/2.5/2.5, v/v/v). The peptide solution was collected and precipitated with cold ether. The precipitates were recrystallized and purified by high-performance liquid chromatography (HPLC).

2.2 Peptide hydrogel preparation

Peptide hydrogels were prepared via a photocrosslinking method using dityrosine-containing peptides. The peptides were dissolved in 0.05 M NaOH solution, and the pH was adjusted to neutral to form the precursor solution. Freshly prepared solutions of $Ru(bpy)_3Cl_2$ (0.1 mol%) and ammonium persulfate (APS, 2 eq.) were added, followed by gentle vortexing to ensure homogeneity. The reaction mixture (typically 200 μL per sample) was then exposed to 405-nm visible light using a custom-built photoreactor equipped with light-emitting diodes (LEDs). The irradiation was performed at an illumination distance of 5 mm with a light intensity of 112 $mW\cdot cm^{-2}$, ensuring uniform exposure across the reaction area under constant current conditions. Photocrosslinking was carried out for up to 5 min to form peptide hydrogels.

2.3 Critical aggregation concentration determination

The critical aggregation concentration (CAC) of the de novo designed peptides was determined using the Nile red method, which involves measuring fluorescence intensity at the maximum emission wavelength with varying peptide concentrations. A 1 mM pre-gel stock solution was prepared and serially diluted to obtain eight groups of peptide solutions ranging from 7.8 μM to 1 mM. Each 1 mL peptide solution was mixed with 10 μL of a Nile Red stock solution in ethanol (250 μM), resulting in a final Nile Red concentration of 2.5 μM. The solutions were gently mixed by aspiration with a pipette. Fluorescence spectra were recorded using a fluorescence spectrometer, with emission wavelengths from 400 to 800 nm at 5 nm intervals, and an excitation wavelength of 550 nm. The fluorescence intensity at the maximum emission wavelength for each peptide was calculated using the equation (Eq. (1)).

$$I_{\text{F, Corrected}} = I_{\text{F, Peptide}} - I_{\text{F, NileRed}} \tag{1}$$

where $I_{\text{F, Peptide}}$ is the triplicate average fluorescence intensity of the sample, and $I_{\text{F, Nile Red}}$ is the fluorescence intensity of Nile Red in water without the peptide. The CAC value of each peptide was then estimated through graph fitting.

2.4 ThT fluorescence analysis

A stock solution was prepared by dissolving thioflavin T (ThT) in deionized water to a concentration of 40 μM, followed by thorough vortexing. For the experiment, 500 μL of peptide hydrogel (0.2 $mg\cdot mL^{-1}$) was combined with an equivalent volume of ThT solution in a 2 mL centrifuge tube. The mixture was homogenized by pipetting in darkness for approximately 10 s. A control solution was prepared by diluting ThT with deionized water. The fluorescence emission spectrum, ranging from 400 to 600 nm, was measured using an excitation wavelength of 420 nm.

2.5 *In vitro* degradation of peptide hydrogels

Hydrogel degradation was assessed by monitoring mass loss over time under physiological (pH 7.4) and mildly acidic (pH 6.0) conditions. Briefly, 1.0 wt.% 4Y6F hydrogel samples (0.5 mL) were incubated with an equal volume of phosphate-buffered saline (PBS) at 37 °C. The incubation medium was refreshed every 24 h to maintain sink conditions. At designated time points, the residual hydrogel mass was recorded, and the degradation rate was calculated as the ratio of the remaining mass to the initial mass.

2.6 Rheological characterization of peptide hydrogel

The rheological properties of the peptide hydrogels were characterized using an Anton Paar MCR502 rheometer. Strain scanning tests were conducted to determine the linear viscoelastic region within the strain range of 0.1%–100%. Dynamic frequency sweeps were performed at a strain amplitude of 1.0% across a frequency range of 0.1–10 $rad\cdot s^{-1}$ to observe the changes in the storage modulus and loss modulus of the hydrogels. The self-healing test was conducted using a simple cut-link model. Initially, a low constant strain of 1% was applied and monitored for a few minutes, followed by a sudden increase to a higher strain of 100% for a few minutes.

2.7 Macroscopic autonomous self-healing and adhesion studies

The self-healing and adhesive capabilities of peptide hydrogel were validated through direct visual observation. Initially, two square blocks of hydrogel were prepared using molds, with one block stained with rhodamine B to enhance visibility. These blocks were then bisected along the median, and the resulting halves were fused without any external stimulus. Following a designated duration, the hydrogel reverted to its original configuration, enabling manipulation of the entire structure by holding one end. Additionally, the adhesion of peptide hydrogel was examined on various *ex vivo* biological tissues, including commercially sourced, defatted pig skin, and mouse organs such as the heart, liver, spleen, lung, and kidney. The pig skin was cut into 2 cm by 3 cm rectangles. Hydrogel blocks were then placed on these samples with slight pressure to ensure contact; adherence was subsequently monitored. Digital photographs recorded the hydrogel's self-healing and adhesive properties.

2.8 Free radical scavenging assessment

This study utilized 2,2-diphenyl-1-picrylhydrazyl (DPPH) and 2,2'-azino-bis(3-ethylbenzothiazoline-6-sulfonic acid) diammonium salt (ABTS) methods to determine the free radical scavenging activity of peptide hydrogels, specifically their capacity to neutralize reactive oxygen species (ROS). For the DPPH assay, peptide hydrogel precursor solutions at varying concentrations and a control were incubated with 100 μM DPPH in equal volumes for 30 min in a 96-well plate with three replicates per group. Absorbance was measured at 517 nm. The clearance rate was calculated according to Eq. (2).

$$\text{Clearance rate}\ (\%) = [(A_s - A_n)/A_s] \times 100 \tag{2}$$

where A_s is the ultraviolet (UV) absorbance of the DPPH-only control and A_n is the absorbance of the experimental groups.

Simultaneously, an ABTS assay was conducted by mixing 2.84 $mg\cdot mL^{-1}$ ABTS in ethanol with 0.664 $mg\cdot mL^{-1}$ potassium persulfate in a 1:1 ratio. After resting in the dark for 15 h, the mixture was diluted with absolute ethanol to achieve an absorbance of 0.7 ± 0.02 at 734 nm. The experimental protocol was identical to that of the DPPH assay.

2.9 *In vitro* antibacterial ability evaluation

The antimicrobial properties of peptide hydrogel were evaluated utilizing the Gram-positive bacteria *Staphylococcus aureus* (*S. aureus*, ATCC 6538), Gram-negative bacteria *Escherichia coli* (*E. coli*, ATCC 8739), and methicillin-resistant *Staphylococcus aureus* (MRSA, ATCC 43300) as model bacteria. Initially, 1 mL of peptide hydrogel at varying concentrations was mixed with 1 mL of bacterial suspension (2×10^6 $CFU\cdot mL^{-1}$) and incubated at 37 °C for 8 h. The antibacterial activity was assessed using the spread plate method. Each sample, diluted 1×10^4-fold, was uniformly plated onto tryptone soy agar (TSA) plates and incubated for an additional 24 h. Following this period, the plates were photographed to document colony growth. Colony-forming units were counted, and the bacterial survival rate was quantified by comparing the number of colonies in the hydrogel-treated samples to those in the PBS control group.

2.10 Outer membrane permeabilization study

The ability of the synthesized peptide 4Y6F and 10Y to permeabilize bacterial outer membranes was assessed using an 1-*N*-phenylnaphthylamine (NPN) fluorescence-based method. Bacterial strains were centrifuged at 3500 rpm for 3 min, and the resulting pellets were collected, washed twice with PBS, and resuspended in PBS buffer. NPN was then added to the bacterial suspensions (2×10^6 $CFU\cdot mL^{-1}$) to a final concentration of 10 μM, followed by incubation at 37 °C for 30 min. Subsequently, 100 μL of peptide hydrogel (10 $mg\cdot mL^{-1}$) was introduced, and the mixture was further incubated for 1 h. Fluorescence intensity (λ_{ex}: 350 nm, λ_{em}: 420 nm) was continuously monitored for 1000 s to track changes in membrane permeability.

2.11 Cytoplasmic membrane depolarization study

Bacterial suspensions (2×10^6 $CFU\cdot mL^{-1}$) in PBS buffer were incubated with 0.4 μM 3,3'-dipropylthiacarbocyanine iodide ($DiSC_3(5)$) for 1 h. After incubation, 100 mM potassium chloride was added to equilibrate the intracellular and extracellular K^+ concentrations. Following hydrogel formation, test peptides were added to the bacterial solutions at a final concentration of 10 $mg\cdot mL^{-1}$. The fluorescence signal (λ_{ex}: 622 nm, λ_{em}: 670 nm) was continuously monitored for 1000 s to evaluate changes in membrane potential.

2.12 Membrane oxidation (malondialdehyde (MDA)) assay

Peptide pre-gel solutions were co-incubated with bacterial suspensions at 37 °C for 12 h. Bacterial pellets were collected by centrifugation, lysed by sonication in extraction buffer, and clarified by centrifugation. The supernatants were reacted with the MDA working reagent according to the manufacturer's instructions, heated at 100 °C for 1 h, cooled to room temperature, and analyzed by measuring absorbance at 532 and 600 nm. MDA concentrations were calculated following the kit protocol.

2.13 Cell viability assay

Mouse embryonic fibroblast (NIH 3T3) cells, sourced from KeyGEN Biotech, were used to evaluate the biocompatibility of de novo designed peptides. The cells were cultured in high-glucose Dulbecco's modified Eagle medium (DMEM) supplemented with 10% fetal bovine serum (FBS) and 1% Penicillin-Streptomycin under conditions of 37 °C, 5% CO_2, and 95% humidity. Viability was quantitatively assessed using the 3-(4,5-dimethylthiazol-2-yl)-2,5-diphenyltetrazolium bromide (MTT) assay. Cells were seeded at

3×10^3 per well in 96-well plates and cultured to achieve over 90% adhesion after 24 h. The control group was maintained in DMEM buffer, while the experimental group was treated with various concentrations of peptide hydrogel precursor solutions. On days 1, 3, and 5, the medium was replaced with 100 μL of 5 mg·mL^{-1} MTT in PBS per well, and the plates were incubated at 37 °C in the dark for 4 h. Absorbance at 490 nm was measured using an Enspire multimode microplate reader (PerkinElmer). Cell viability percentage was calculated by comparing the optical density variations between the experimental and control groups, normalized against a blank.

2.14 Live/dead cell assay

For observations of live and dead cells, NIH 3T3 cells were seeded at 1×10^4 cells per well in 35-mm glass bottom confocal dishes. After overnight incubation, the cells were treated with peptide hydrogel precursor solutions (1 wt.%) and cultured for 1, 3, and 5 days. After each incubation period, the culture medium was removed, and the cells were stained with calcein-AM/propidium iodide (PI) for 30 min. The stained cells were subsequently imaged using a confocal laser scanning microscope (CLSM, Leica TCS-SP5).

2.15 Hemolysis assay

The hemolytic activity of the peptide hydrogel was evaluated using mouse red blood cells (RBCs). Fresh blood was collected from mice via ocular extraction, and erythrocytes were isolated by centrifuging at 1500 rpm for 10 min. The RBCs were washed three times with PBS and then resuspended in PBS for testing. Equal volumes of the blood solution and peptide solutions, ranging from 0.063 wt.% to 1 wt.%, were mixed. After a 2-h incubation at 37 °C, the mixtures were centrifuged at 3000 rpm for 10 min to separate supernatants. A 200 μL aliquot of each supernatant was transferred to a 96-well plate, and absorbance was measured at 545 nm using a microplate reader. The hemolysis ratio was determined by comparing the absorbance of the peptide-treated samples to that of control samples, with adjustments for baseline absorbance differences.

2.16 Cell migration study

To evaluate the effect of the hydrogel on cell migration, NIH 3T3 cells were seeded at 1×10^5 per well in 6-well plates and cultured to 90% confluency. A straight vertical scratch was made using a 200 μL pipette tip. The cells were then incubated with DMEM medium containing peptide hydrogel (0.1 wt.%) for 24 and 48 h. After treatment, the cells were fixed with 4% paraformaldehyde for 20 min. The resulting cell scratches were then visualized using an optical inverted microscope, and the gap areas were quantified with ImageJ for migration analysis.

2.17 Intracellular ROS scavenging assessment

NIH 3T3 cells were seeded at a density of 5×10^3 per confocal dish and incubated for 24 h to allow cell attachment. The cells were then treated with 0.25 wt.% peptide hydrogels in the presence of 100 μM H_2O_2. Cells treated with PBS served as the negative control, while cells exposed solely to 100 μM H_2O_2 formed the positive control. After 6 h, the cells were washed three times with PBS and then incubated with the 2-(3,6-diacetoxy-2,7-dichloro-9H-xanthen-9-yl) benzoic acid (DCFH-DA) ROS probe for 30 min. Intracellular ROS levels were visualized using a CLSM, and mean fluorescence intensity was quantified by ImageJ software.

2.18 *In vivo* infected wound healing

Female BALB/c mice (aged 6–8 weeks) were obtained from the Animal Care Unit at Capital Medical University, in accordance with protocols approved by the Animal Ethics Committee of Capital Medical University. To assess the antibacterial and wound healing properties of peptide hydrogels *in vivo*, full-thickness skin defect models infected with bacteria were established in the mice. Mice were anesthetized by intraperitoneal injection of 1.25% tribromoethanol (0.2 mL per 10 g body weight), and an 8 mm diameter full-thickness excisional wound was created on the dorsal skin, followed by inoculation with 200 μL of MRSA suspension (1×10^8 CFU·mL^{-1}). The mice were subsequently randomized into five treatment groups: PBS (blank group), Prontosan® commercial dressing (control), and three 1 wt.% peptide hydrogel formulations (4Y6F, 10F, and 10Y). The hydrogels were applied to cover the wounds and replaced every 3 days during the early treatment stage, with earlier replacement performed when loosening, excessive exudate, or contamination was observed; residual hydrogel was gently removed and fresh hydrogel was reapplied at each replacement. Wound progression was monitored through digital photographs taken on days 0, 3, 7, and 12 post-operations, and wound areas were measured with ImageJ software. Residual wound area percentages were calculated using the equation (Eq. (3)).

$$\text{Residual wound area }(\%) = \left(\frac{\text{Wound area at each time point}}{\text{Initial wound area}}\right) \times 100 \tag{3}$$

On day 4, bacterial colonies from the wound sites were cultured on agar plates to evaluate the treatments' antibacterial efficacy. On day 12, the mice were euthanized, and wound tissues were collected for histological examination, including hematoxylin and eosin (H&E) staining, Masson's trichrome staining, immunofluorescent staining of cluster of differentiation 31 (CD31) and alpha-smooth muscle actin (α-SMA), immunohistochemical staining of tumor necrosis factor-alpha (TNF-α) and interleukin-6 (IL-6), as well as collection of blood samples and major organs for hematological and histological examination.

2.19 *In vivo* degradation and long-term biosafety evaluation

To evaluate *in vivo* degradation behavior and long-term biosafety, two parallel subcutaneous implantation studies were performed. For *in vivo* degradation tracking, a 1.0 wt.% 4Y6F peptide hydrogel encapsulating rhodamine 800 was implanted into a dorsal subcutaneous pocket of BALB/c mice via a small longitudinal incision, which was subsequently sutured. Mice in this group were imaged weekly using near-infrared fluorescence on a PerkinElmer IVIS Spectrum system. In parallel, another group of mice received subcutaneous implantation of the 4Y6F peptide hydrogel. Body weight was recorded during the 8-week observation. At the end of the experiment, mice were euthanized, and major organs were collected for H&E staining.

3 Results and discussion

3.1 De novo peptide design and fibrillization behavior

In designing peptide sequences for hydrogels, hydrophobic FF and hydrophilic YY motifs were incorporated as the fibril skeleton to exploit the synergistic characteristics of covalent and non-covalent interactions inherent in this peptide platform. The structural similarity between F and Y, differing only by a phenolic hydroxyl group, provides a unique opportunity to explore structure-function relationships and their impact on hydrogel properties. Drawing on prior experience, we de novo designed a series of 18-mer peptides (Figs. 1(a) and 1(b)) by carefully optimizing parameters such as chain length, molecular weight and rigidity, and the balance between hydrophilicity and hydrophobicity. These peptides featured five interchangeable FF/YY segments interconnected by four alternating DX residue sets. Within this platform, negatively charged D residues bearing polycarboxyl structure acted as hydrophilic/ionic regulators; flexible and hydrophobic X spacers modulated molecular rigidity, promoting enhanced peptide entanglement and the extension of assembled structures; and N-terminal acetylation minimized the formation of intramolecular zwitterions, ensuring structural stability. Using the peptide sequence YYXDYYDXYYXDYYDXYY (10Y) as the starting template, we replaced the five YY segments stepwise to achieve a gradient substitution, culminating in the de novo design of peptides: YYXDYYDXFFXDYYDXYY (8Y2F), YYXDFFDXYYXDFFDXYY (6Y4F), FFXDYYDXFFXDYYDXFF (4Y6F), FFXDFFDXYYXDFFDXFF (2Y8F), and FFXDFFDXFFXDFFDXFF (10F). This progressive substitution allows precise control over the balance between FF fibrillization and YY photochemical crosslinking, facilitating fine-tuned adjustments from peptide structure to hydrogel functionality.

Synthetically, these de novo designed peptides were sequentially prepared on CTC resin using standard solid-phase peptide synthesis (SPPS), and their chemical structures were meticulously confirmed by ^{1}H NMR (nuclear magnetic resonance) and HR-ESI MS (high-resolution electrospray ionization mass spectrometry) (Figs. S1–S14 in the ESM). Taking the 4Y6F peptide as an example, all 158 protons were clearly resolved in the ^{1}H NMR spectrum (Fig. 1(c)), confirming complete structural integrity. Additionally, the polycarboxyl and polyphenolic hydroxyl groups within the peptide structure yielded exceptional characterization in mass spectrometry (Fig. 1(d)), a doubly charged molecular anion $[M-2H]^{2-}$ was observed at m/z = 1253.0655 (err. +5.27 ppm) with coordinating capability to four Na$^+$ cations.

For hydrogel fabrication, the degree of peptide fibrillization is a critical prerequisite parameter [66–68], as it reinforces hydrophobic interactions and consequently promotes bacterial membrane permeation [69–71], which can be evaluated by analyzing the self-assembly behavior of the synthesized peptides prior to photofabrication. Transmission electron microscopy (TEM)-based microstructural characterization revealed distinct morphological features influenced by the FF/YY content in the peptide sequences (Fig. 1(g)). Peptides with low FF content (e.g., 10Y, 8Y2F, 6Y4F) exhibited sparse and loose nanofiber networks interspersed with droplet-like aggregates and membranous structures attached to fibril intersections. This morphology was attributed to aromatic π-π stacking and the limited hydrogen bonding capacity of tyrosine. As the FF content increased, the fibers transitioned to denser, more

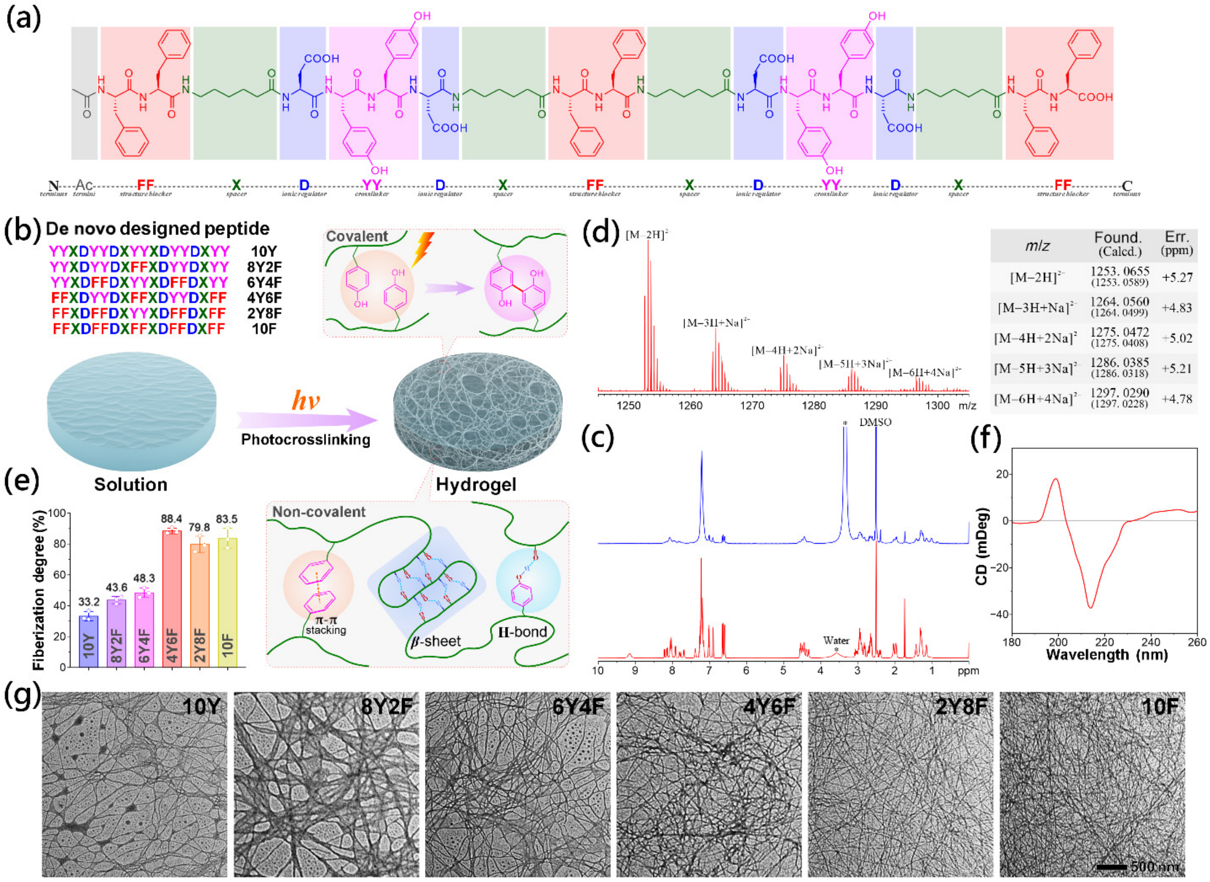

m/z	Found. (Calcd.)	Err. (ppm)
$[M-2H]^{2-}$	1253.0655 (1253.0589)	+5.27
$[M-3H+Na]^{2-}$	1264.0560 (1264.0499)	+4.83
$[M-4H+2Na]^{2-}$	1275.0472 (1275.0408)	+5.02
$[M-5H+3Na]^{2-}$	1286.0385 (1286.0318)	+5.21
$[M-6H+4Na]^{2-}$	1297.0290 (1297.0228)	+4.78

Figure 1 (a) De novo designed peptides. (b) Schematic representation of peptide hydrogel formation under visible light irradiation. (c) ^{1}H NMR spectra of 4Y6F peptide before (bottom, in DMSO-d_6) and after (top, in DMSO-d_6/D$_2$O, 9/1) irradiation. (d) HR-ESI MS spectrum and analysis of 4Y6F peptide. (e) Fiberization degree of peptide assemblies. (f) CD spectrum of 4Y6F peptide solution. (g) TEM images of peptide assemblies.

compact configurations, accompanied by a reduction in droplet-like aggregates and membranous structures. By 4Y6F, highly intertwined nanofibers less than 26 nm in width were observed. For sequences 2Y8F and 10F, the fibrils evolved into a denser and more cohesive network, with diameters ranging from 9 to 46 nm. Interestingly, these changes in anionic strength were corroborated by mass spectrometry (Figs. S1, S3, S5, S7, S9, and S11 shown in the ESM). In the gradient peptide system (from 10Y to 10F), the binding strength of the doubly charged molecular anion to multiple Na^+ cation progressively decreased, with the coordination number reducing from 7 to 3. This trend can be clearly attributed to the combined influence of the four negatively charged D residues and the decreasing YY motifs. To quantitatively evaluate peptide fibrillization, TEM images were analyzed using a histogram-based treatment [72]. Fibrous assemblies were distinguished from the amorphous background by threshold-based image processing, and their pixel areas were quantified. The degree of fibrillization was then defined as the ratio of the fibrillar area to the total hydrogel area, providing a reproducible metric for network formation. In our de novo designed peptide platform, the fibrillization degree showed a steady increase from 33.2% for 10Y to 43.6% for 8Y2F and 48.3% for 6Y4F (Fig. 1(e)). A sharp increase was observed at 4Y6F, reaching 88.4%, marking a clear inflection point. Beyond this, the fibrillization degree stabilized, plateauing at a threshold value of approximately 80%. These results underscore the critical balance between FF and YY content in driving fibrillization and forming robust nanofiber networks essential for hydrogel functionality.

The fibrillization propensity of peptides could be further quantified by measuring their CAC [73]. In our gradient peptide system, increasing FF content corresponds to a decrease in CAC values, ranging from 124 o 68.7 μM (Fig. S15 in the ESM). This propensity, observed across peptides with comparable molecular weights, arises from the synergistic interplay between in-plane β-sheet extension and out-of-plane aromatic π-π stacking.

Higher-order peptide assemblies can be further evaluated using circular dichroism (CD) spectroscopy. In our gradient peptide platform, the peptides exhibit a characteristic strong negative band at 210 nm and an intense positive peak at 200 nm (Fig. 1(f) and Fig. S16 in the ESM), indicative of β-sheet-related secondary structures driven by extensive intermolecular and intrastrand hydrogen bonding [22, 62, 74]. Across the gradient from 10Y to 10F, increasing FF content corresponds to higher maxima and deeper minima, accompanied by a blue shift of approximately 5 nm in both bands. This shift suggests increasingly twisted and distorted β-sheet arrangements as FF content rises. Complementary fluorescence spectroscopy using ThT as a specific indicator for β-sheet assemblies further supports these findings, higher FF content leads to stronger fluorescence signals (Fig. S17 in the ESM), confirming enhanced β-sheet formation and improved structural organization facilitated by aromatic π-π stacking within the peptide assemblies [16].

3.2 Photofabrication and properties of peptide hydrogels

Peptide hydrogels were successfully prepared via a one-pot photochemical approach from de novo designed peptide solutions. Gelation occurred in aqueous media under near-neutral conditions at pH 6 and was rapidly initiated with 405-nm LEDs (112 mW·cm^{-2}), completing within 5 min. The mechanism underlying gel formation is attributed to the photochemical crosslinking of dityrosine through photoinduced tyrosyl radical coupling reactions. Gel-inversion experiments demonstrated that hydrogel formation depended on the initial peptide concentration and was significantly modulated by the interplay between FF and YY residues. Peptides with high YY content, such as 10Y and 8Y2F, exhibited a minimum gelation concentration (MGC) of approximately 0.25 wt.%. Intermediate compositions like 6Y4F and 4Y6F demonstrated even lower MGCs of 0.12 wt.% and 0.10 wt.%, respectively. For peptide 2Y8F with increased FF content, the MGC rose to 0.18 wt.%, while fully FF-based peptide 10F displayed thermoresponsive dissolution with an MGC of 0.40 wt.%. These findings illustrate a gradient peptide platform where covalent photochemical crosslinking of YY residues and non-covalent fibrillization driven by FF residues work synergistically to facilitate the photofabrication of peptide assemblies and significantly lower the concentration of gelation threshold. As a control, peptide 5Y5F, composed of five alternating FY segments, exhibited a substantially higher MGC of 0.5 wt.%. This alternating arrangement of hydrophobic F and hydrophilic Y residues would disrupt the cooperation between π-π stacking and hydrophilic-hydrophobic assembly, further emphasizing the essential role of both double FF-driven fibrillization and double YY-mediated photochemical crosslinking in hydrogel photofabrication and optimization (Fig. 1(b)).

Given the exceptional gelation performance, optimized 4Y6F peptide was selected for detailed analysis of hydrogel properties. As shown in Fig. 2(a), a clear aqueous solution of 4Y6F gradually solidified into an immobile hydrogel within 5 min of visible light irradiation, forming a stable network structure (Fig. 2(b)). This process was monitored by fluorescence spectroscopy, where a prominent emission peak at around 410 nm emerged within the same time frame, corresponding to the formation of dityrosine bonds (Fig. 2(c)). Structural changes in 4Y6F were further confirmed by ^{1}H NMR spectra (Fig. 1(d)), showing significant peak broadening and merging after irradiation, indicative of polymeric characteristics. Specifically, the para-substituted aromatic proton peaks at 6.59 and 6.91 ppm exhibited reduced intensity, reflecting the conversion of YY residues into dityrosine dimers (2.84%) and their spatial confinement (67.0%) within the photochemically crosslinked 3D network. Morphological changes were visualized using TEM and scanning electron microscopy (SEM) (Figs. 2(d) and 2(e), and Fig. S18 in the ESM). After irradiation, 4Y6F displayed a 3D nanofibrillar network characterized by entangled and branched nodes, forming an interconnected and porous structure. SEM images of freeze-dried hydrogels revealed a porous structure with well-ordered pores averaging ~ 45 μm. This robust nanostructure was most pronounced in peptide systems with high or intermediate YY content, while peptides with high FF content, such as 2Y8F and 10F, exhibited minimal morphological changes due to the lack of photoreactive YY residues.

Fourier transform infrared (FT-IR) spectroscopy further characterized the peptide hydrogels (Fig. 2(i) and Fig. S19 in the ESM), identifying obvious function groups including hydroxyl (3280 cm^{-1}), alkyl methylene (2930 cm^{-1}), amide I (1640 cm^{-1}), amide II (1515 cm^{-1}), phenyl-O stretching (1170 cm^{-1}), and aromatic ring bending (800–860 cm^{-1}). Deconvolution of the amide I region (1600–1700 cm^{-1}) revealed absorption peaks associated with β-sheet and β-turn conformations (Fig. 2(j) and Fig. S20 in the ESM) [75]. Quantitative analysis showed that photo-crosslinked 4Y6F assemblies had the highest β-secondary structure content at 34% (Table S1 in the ESM), attributed to the interplay of chemical

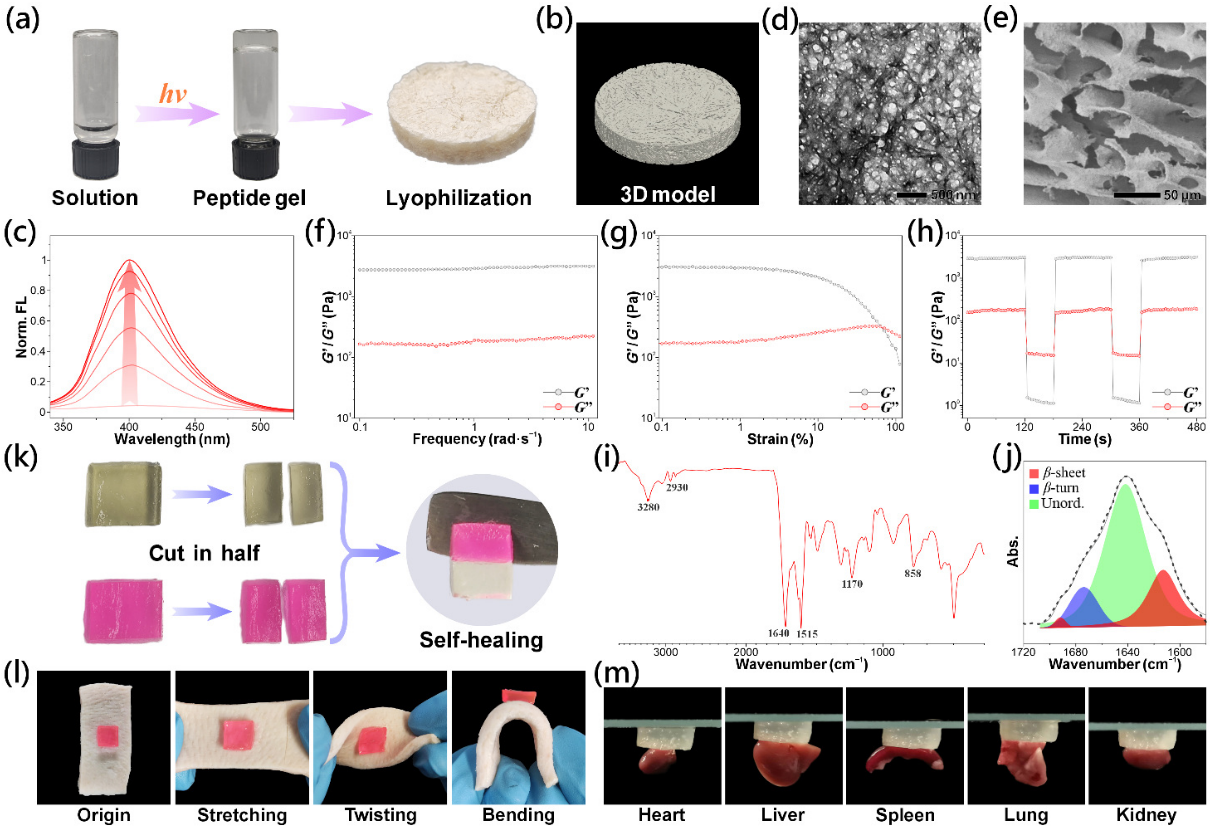

Figure 2 Characterizations of 4Y6F peptide hydrogel. (a) Photocrosslinking of 4Y6F peptide hydrogel in a vial and its freeze-dried form. (b) X-ray computed tomography (CT)-based 3D reconstruction of 4Y6F peptide hydrogel. (c) Fluorescence emission spectra for 4Y6F peptide upon visible light irradiation of 0, 2, 4, 6, 8, 10 min. (d) TEM and (e) SEM images of 4Y6F peptide hydrogel. (f) Frequency sweep (0.1–10 $\mathrm{rad \cdot s^{-1}}$) of 1 wt.% hydrogel. (g) Strain sweep (0.1%–100%) of 1 wt.% hydrogel. (h) Oscillatory rheology under alternating high and low strains. (i) FT-IR spectra of the hydrogel. (j) Quantitative analysis of the secondary structures with Gaussian curve fitting in FT-IR spectra. (k) Images of the self-healing process. (l) Adhesion of the hydrogel on porcine skin under deformations. (m) Adhesion of the hydrogel on rat organs.

bonding and physical interactions during gelation. *In vitro* degradation experiments at pH 7.4 and 6.0 revealed a gradual mass loss of the 4Y6F hydrogel, with degradation approaching completion within approximately three weeks and proceeding slightly faster under mildly acidic conditions (Fig. S21 in the ESM).

Rheological experiments were performed to characterize the mechanical properties of the 4Y6F peptide hydrogel. As depicted in Fig. 2(f), frequency sweeps revealed a storage modulus (G') of ~ 3000 Pa, consistently greater than the loss modulus (G''), confirming its gel-like behavior. Across different peptide concentrations, the storage modulus of the 4Y6F hydrogel (G' ~ 0.6–8.0 kPa) is comparable to that reported for representative self-assembling peptide-based hydrogels, which typically exhibit G' values ranging from several hundred pascals to several kilopascals (Fig. S22 in the ESM). Notably, this modulus range overlaps with that commonly associated with soft tissues, supporting the mechanical relevance of the 4Y6F hydrogel. During strain sweeps, shear-yielding behavior was observed, with the G'/G'' crossover occurring around 40% strain (Fig. 2(g)). When subjected to alternating low (1%) and high (100%) shear strains, the hydrogel displayed an inversion of the moduli at high strain (Fig. 2(h)), indicating liquid-like behavior, while the rapid restoration of G' at low strain demonstrated its self-recovery capability [76].

The self-healing properties of the 4Y6F hydrogel were evaluated using two gel blocks, one stained with rhodamine B for visual contrast. After being halved and rejoined, the sections adhered within 5 min to an integral block (Fig. 2(k)). The repaired hydrogel withstood lifting without splitting, indicating sufficient interaction forces to support its own weight. Additionally, the 4Y6F hydrogel showed strong adhesion to porcine skin and rat organs (Figs. 2(l) and 2(m)), maintaining firm attachment under various degrees of locomotion and effectively supporting organ weight. This performance was attributed to the formation of strong hydrogen bonds with tissue surfaces.

3.3 Antibacterial activity and mechanism of the peptide hydrogels

Bacterial infection is a major challenge in biomedicine, particularly in wound healing, where peptide hydrogels can serve as effective barriers against microbial invasion [8, 70]. Using agar plate count assays and minimum inhibitory concentration (MIC) analysis against key pathogens, including *S. aureus*, MRSA, and *E. coli*, broad-spectrum antibacterial activity against both Gram-positive and Gram-negative bacteria by the de novo designed peptide hydrogels was evaluated. As shown in Figs. S23 and S24 in the ESM, MIC values revealed a strong correlation between FF content and antibacterial efficacy. For MRSA, the hydrogel 10Y, lacking FF residues, exhibited weak inhibitory activity (Figs. 3(a) and 3(b)). In contrast, hydrogels with increasing FF content, from 8Y2F to 10F, demonstrated a progressive decrease in MIC values, from 32.0 to 4.00 $\mathrm{mg \cdot mL^{-1}}$ (Table S2 in the ESM). The identical MIC values

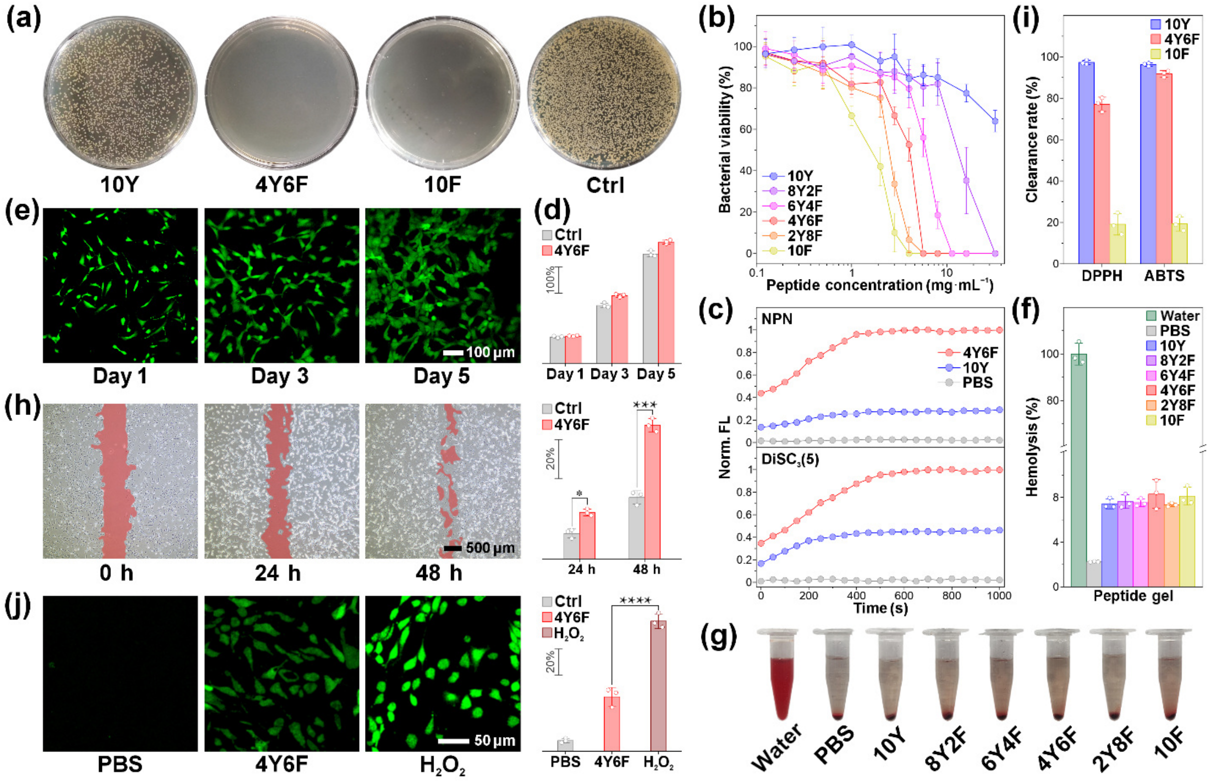

Figure 3 *In vitro* evaluation of the antibacterial, biocompatibility, and antioxidant properties of peptide hydrogels. (a) Agar plate images of MRSA treated with 5.65 mg·mL^{-1} of 10Y, 4Y6F, and 10F peptide hydrogels. (b) Antimicrobial activities of peptide hydrogels against MRSA ($n = 3$). (c) Permeabilization (top) and depolarization (bottom) effects of 4Y6F and 10Y peptide hydrogels on MRSA cell membranes. (d) MTT cytotoxicity evaluation and (e) Live/dead staining of NIH 3T3 cells treated with 4Y6F peptide hydrogel (1 wt.%) at days 1, 3, and 5 ($n = 3$). (f) and (g) Hemolysis ratio and representative hemolysis images of peptide hydrogels (1 wt.%); water, positive control; PBS, negative control ($n = 3$). (h) Migration and quantitative analyses of NIH 3T3 cells incubated with 4Y6F peptide hydrogels (0.1 wt.%) for 24 and 48 h ($n = 3$, $^{**}P < 0.01$, $^{***}P < 0.001$). (i) DPPH and ABTS free radical scavenging activities of 10Y, 4Y6F, and 10F peptide hydrogels at 2 wt.% ($n = 3$). (j) CLSM images and intracellular ROS scavenging analyses in NIH 3T3 cells treated with 4Y6F peptide hydrogels ($n = 3$, $^{****}P < 0.0001$).

obtained for different bacterial strains reflect antibacterial assessment conducted in a relatively high concentration regime, where concentration-dependent differences are not readily resolved. At the concentration of 5.65 mg·mL^{-1}, peptide hydrogels containing three or more FF groups (4Y6F, 2Y8F, and 10F) showed significant antibacterial activity, with no bacterial colonies observed on agar plates. The antibacterial efficacy was not only associated with the FF content but was more driven by an amplified antimicrobial effect, likely arising from synergistic interactions within the hydrogel network. The contribution of FF does not stem from classical charge-mediated antimicrobial interactions but from enhanced fibrillization and aromatic stacking that facilitate supramolecular, membrane-disruptive behavior. Accordingly, 4Y6F, with three times the FF content of 8Y2F, yielded MIC values five-fold lower.

The primary antibacterial mechanism of FF-containing peptide hydrogels involves targeting bacterial membranes, leading to significant perturbations and morphological damage [69]. To elucidate this mode of action, the ability to induce membrane permeabilization and depolarization was systematically evaluated against the tested bacterial strains in our peptide platform (Fig. 3(c) and Fig. S25 in the ESM). Upon incubation with the 4Y6F hydrogel, significant outer membrane permeabilization was observed, evidenced by fluorescence changes in the NPN dye, a probe that increases fluorescence upon binding to hydrophobic membrane regions. Additionally, rapid depolarization of the inner membrane was also detected as a marked increase in fluorescence intensity of the DiSC$_3$(5) potentiometric probe. In contrast, 10Y peptide, used as a control, induced no significant changes in either NPN or DiSC$_3$(5) fluorescence, consistent with its limited antibacterial activity. To further evaluate membrane oxidative stress, MDA, a lipid peroxidation biomarker, was quantified [77]. All tested strains treated with 4Y6F exhibited significantly elevated MDA levels (Fig. S26 in the ESM), indicative of severe membrane destabilization and further supporting a physical membrane disruption mechanism. These findings, well-aligned with MIC data, demonstrate that the balance between FF and YY content in governing antibacterial functionality, highlighting how peptide design influences hydrogel fabrication and antimicrobial efficacy.

3.4 Biocompatibility and antioxidant properties of the peptide hydrogels

The biocompatibility of peptide hydrogels is a crucial prerequisite for their potential use in various biomedical applications. Cytotoxicity, measured via the MTT assay on NIH 3T3 cells, showed that > 95% of cells remained viable after exposure to peptide solutions at concentrations up to 1.0 wt.% (Fig. S27 in the ESM), a level twice the minimum inhibitory concentration of 4Y6F against bacteria. Notably, cell viability increased by 30% to 50% over a period of 3 to 5 days (Fig. 3(d) and Fig. S28 in the ESM), suggesting the hydrogels' capacity to support and promote cell proliferation. These findings were further validated by live/dead staining, which exhibited bright green fluorescence, minimal dead cells, and well-preserved spindle-shaped cell morphology (Fig. 3(e) and Fig. S29 in the ESM), indicating excellent cytocompatibility throughout the incubation period. Hemolytic activity tests confirmed excellent blood compatibility, with hemolysis rates remaining below 8% at concentrations up to 1.0 wt.% (Figs. 3(f) and 3(g), and Figs. S30 and S31 in the ESM), well within the acceptable threshold for biomedical applications. Additionally, a scratch assay demonstrated enhanced cell migration in the presence of peptide hydrogels; after 24 h, the migration area reached 25% compared to 13% in the control group, progressing further to 68% versus 32% at 48 h (Fig. 3(h) and Fig. S32 and S33 in the ESM). This enhanced migratory capacity is likely attributed to the hydrogels' extracellular matrix-like porous structure and high elastic modulus.

The ability to counteract oxidative stress is another essential factor for biomaterials designed for therapeutic purpose [15, 60, 78]. To evaluate the antioxidant potential of the peptide hydrogels, their free radical scavenging capacity was analyzed, focusing on the contribution of tyrosine-derived phenolic hydroxyl groups. Using two standard tests of DPPH and ABTS, the hydrogels exhibited a concentration-dependent ability to scavenge free radicals, with the exception of 10F due to its lack of tyrosine (Fig. 3(i), and Figs. S34 and S35 in the ESM). At a concentration of 2 wt.%, the hydrogels achieved clearance rates exceeding 67% for DPPH radicals and over 87% for ABTS radicals. Particularly, under comparable concentrations, the hydrogels' antioxidant capacity was found to scale with the tyrosine content in their peptide sequences. Intracellular ROS scavenging was further examined using confocal microscopy. As shown in Fig. 3(j) and Fig. S36 in the ESM, peptide hydrogels at 0.125 wt.% significantly alleviated oxidative stress in NIH 3T3 cells exposed to H_2O_2, as indicated by the quenching of DCFH-DA fluorescence [79]. Quantitative fluorescence analysis confirmed that intracellular ROS scavenging efficiency correlated with the proportion of tyrosine, consistent with trends observed in radical scavenging assays (Fig. S37 in the ESM). YY motif not only supports photocrosslinking but also enhances the antioxidant performance of peptide hydrogels.

3.5 Therapeutic efficacy of the peptide hydrogels

To evaluate their therapeutic efficacy *in vivo*, a full-thickness skin defect mouse model of MRSA infection was employed. This excisional wound healing model allowed the evaluation of epithelialization, inflammation modulation, and angiogenesis, offering comprehensive insights into the antibacterial and tissue regeneration capabilities of the peptide hydrogels. 1 wt.% 4Y6F, 10F, and 10Y peptide hydrogels were selected, alongside a commercial reference hydrogel (Prontosan® gel). On day 3, wounds treated with 4Y6F hydrogel exhibited significant reductions in moisture and size, suggesting effective infection control and early wound healing initiation, whereas yellow pus scattered in the wound beds of other groups signified unresolved infections (Fig. 4(a)). The control group showed minimal improvement, with 62.2% of the initial wound area remaining due to poor infection management over the first 7 days (Fig. 4(b)). Conversely, the 4Y6F group demonstrated superior healing with only 18.6% the wound area remaining, substantially outperforming the 10Y (49.8%), 10F (32.5%), and commercial Prontosan gel (38.8%) groups. This marked improvement reflected enhanced wound repair and reduced inflammation. On day 12, the 4Y6F group achieved near-complete recovery with the formation of an intact epidermis and visible hair regrowth. In comparison, the 10F and Prontosan groups showed minor residual wound areas of 2.5% and 4.6%, respectively, while the 10Y and control groups displayed larger unhealed areas (11.2% and 32.0%, respectively), characterized by persistent wound edges and loosely arranged collagen matrices. To further evaluate the *in vivo* antibacterial efficacy, colony-forming unit (CFU) analysis of wound effusions was conducted on day 7. Consistent with *in vitro* findings, all peptide hydrogel treatments reduced bacterial counts compared to the control, with varying degrees of effectiveness. Notably, the 4Y6F hydrogel achieved nearly complete bacterial elimination, while the 10Y, 10F, and commercial Prontosan groups exhibited bacterial survival rates of 56.5%, 10.7%, and 38.4%, respectively (Fig. 4(c)).

Wound tissue samples were collected on day 12 post-treatment and analyzed using H&E and Masson's trichrome (MTC) staining. As shown in Fig. 4(d) and Fig. S38 in the ESM, wounds treated with 4Y6F peptide hydrogel exhibited the best healing states, with improved epithelialization, hair follicle repair, and denser, more organized collagen deposition. The collagen deposition rate in the 4Y6F group (54.4%) was obviously higher than that of the control (16.2%), 10Y (31.6%), 10F (44.7%), and commercial Prontosan gel (33.7%) groups (Fig. 4(e)), indicating superior matrix remodeling and tissue repair. Additionally, immunohistochemical and immunofluorescence staining were performed to investigate inflammation response and angiogenesis. The expression levels of key pro-inflammatory cytokines IL-6 and TNF-α were markedly reduced in the 4Y6F group (7.8% and 6.6%, respectively), compared to the control (40.8% and 34.1%), 10Y (25.1% and 19.8%), 10F (19.7% and 15.6%), and commercial Prontosan gel (22.0% and 17.6%) groups (Fig. 4(f) and Fig. S38 in the ESM). Similarly, the fluorescence intensity of angiogenesis markers CD31 and α-SMA was significantly elevated in the 4Y6F group relative to all other groups (Fig. 4(g) and Fig. S38 in the ESM), demonstrating enhanced neovascularization. Collectively, these results suggest that the optimized 4Y6F peptide hydrogel effectively accelerates wound healing by modulating the inflammatory phase, promoting re-epithelialization, enhancing collagen deposition, and stimulating angiogenesis.

Biochemical analyses revealed that liver and kidney function indicators, along with hematological parameters, remained within normal ranges in the peptide hydrogel groups after the 12-day treatment period (Figs. S39 and S40 in the ESM). Histological examination of major organs in mice showed well-preserved tissue architecture with no signs of pathological abnormalities (Fig. 4(h) and Fig. S41 in the ESM). To further evaluate *in vivo* degradation behavior, the 4Y6F hydrogel encapsulating rhodamine 800 was utilized for fluorescence tracking, which revealed a gradual attenuation of signal intensity during the early post-implantation stage and complete disappearance by day 21 (Fig. S42 in the ESM), indicating progressive degradation and clearance *in vivo*. In addition, long-term subcutaneous implantation over 8 weeks showed stable body weight profiles and normal organ histology, providing further evidence for favorable long-term *in vivo* tolerance of the peptide hydrogel system (Figs. S43 and S44 in the ESM).

Together with the observed therapeutic efficacy, these results support a favorable *in vivo* safety and degradation profile, while indicating broader applicability of the de novo designed peptide hydrogel platform. Benefiting from its sequence-encodable and modular architecture, this system offers flexibility for incorporating additional functional motifs to address dynamically active tissue environments and complex wound scenarios, as exemplified by

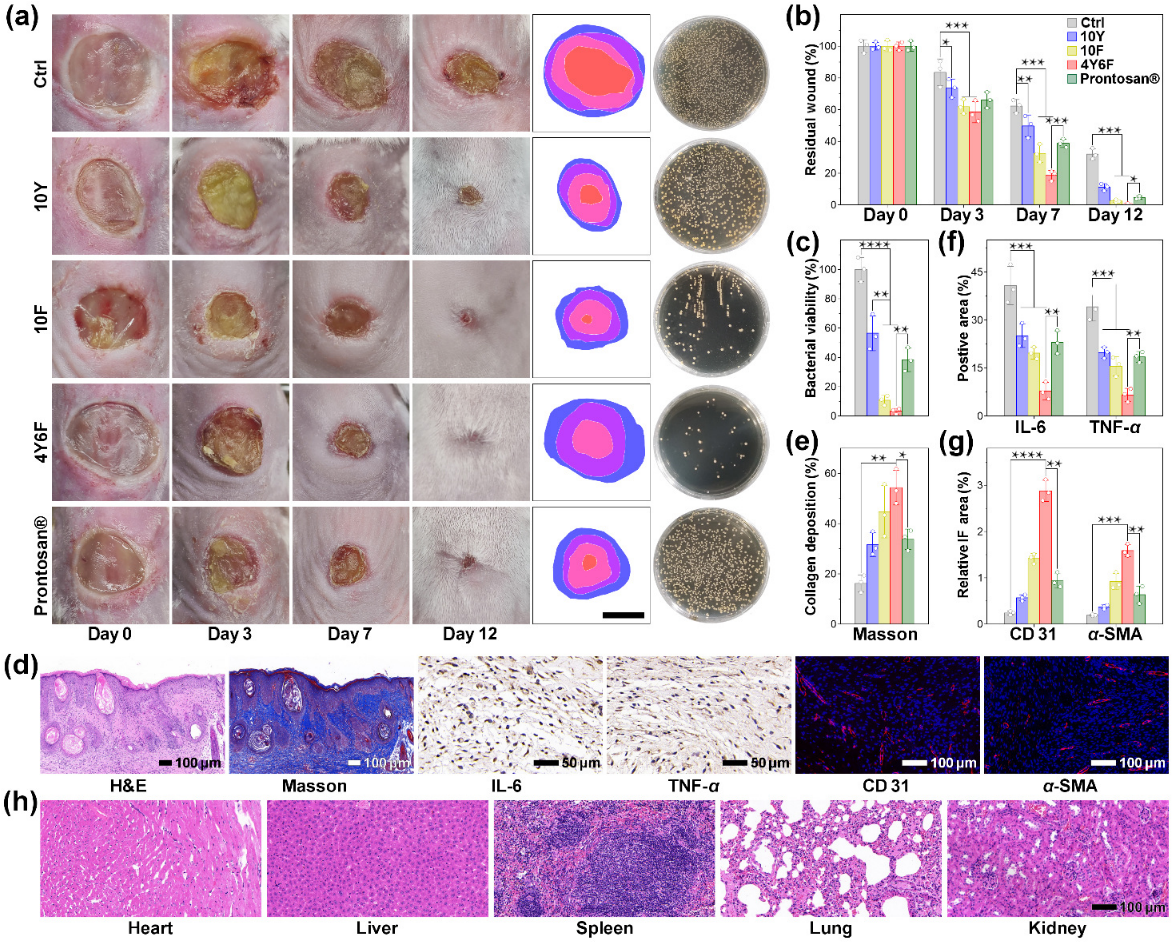

Figure 4 *In vivo* evaluation of the therapeutic efficacy of peptide hydrogels. (a) Representative images of wound healing progression in mice treated with PBS, 10Y, 10F, 4Y6F peptide hydrogels, and commercial Prontosan over 12 days (scale bar: 5 mm). Agar plate images showing MRSA colonies isolated from wound tissues of different groups on day 7. (b) Wound size analysis over 12 days, normalized to the initial size on day 0 ($n = 3$, $^{*}P < 0.05$, $^{**}P < 0.01$, $^{***}P < 0.001$). (c) Quantitative analysis of MRSA colonies from wound tissues across treatment groups ($n = 3$, $^{**}P < 0.01$, $^{****}P < 0.0001$). (d) H&E, Masson, immunohistochemistry (IL-6 and TNF-*α*) and immunofluorescence (CD31 and *α*-SMA) staining of wound tissues after 12-day treatment with 4Y6F peptide hydrogel. Quantitative analysis of (e) collagen deposition, (f) positive staining area (IL-6 and TNF-*α*), and (g) relative immunofluorescence area (CD31 and *α*-SMA) ($n = 3$, $^{*}P < 0.05$, $^{**}P < 0.01$, $^{***}P < 0.001$, $^{****}P < 0.0001$). (h) H&E-stained tissue sections of major organs following 12-day treatment with 4Y6F peptide hydrogel.

multifunctional hydrogel systems for mechanically responsive wound management and soft biointerfaces [80, 81]. Moreover, the mild visible-light-triggered fabrication strategy provides spatiotemporal control over gelation, enabling *in situ* forming and patterned hydrogels compatible with localized therapeutic applications [82].

4 Conclusions

In summary, we fabricated biofunctional peptide hydrogels directly from de novo-designed peptide sequences via visible-light photocrosslinking. Structurally, these peptides synergistically incorporated photochemically crosslinkable dityrosine and self-assembling diphenylalanine motifs, interconnected by alternating hydrophilic L-aspartate and hydrophobic ε-aminocaproic acid residues to optimize amphiphilicity and balance non-covalent fibrillization with covalent crosslinking. Upon visible-light irradiation, the peptides rapidly underwent photocrosslinking in aqueous media, forming hydrogels within five minutes. The resulting hydrogels exhibited tunable gelation properties, robust mechanical stability, and adjustable functionality, with tyrosine-dependent antioxidant capacity finely modulated by the interplay of the FF and YY configurations. Biocompatibility evaluations confirmed excellent cell viability, enhanced cellular proliferation, and negligible hemolytic activity, supporting their safety for biomedical use. *In vivo* wound healing studies over 12 days revealed significantly accelerated re-epithelialization in mice treated with an optimized 4Y6F peptide hydrogel, attributed to enhanced collagen deposition, improved angiogenesis, and reduced inflammation, outperforming both control groups and the commercial Prontosan gel. Fluorescence tracking demonstrated complete hydrogel degradation within 21 days, indicating excellent biometabolic clearance. Collectively, this research introduced a versatile and innovative peptide platform for the photochemical fabrication of hydrogels, effectively bridging de novo design with practical applications in antibacterial therapy and wound healing, and offering a promising bottom-up approach for a wide range of biomedical scenarios.

Electronic Supplementary Material: Supplementary material (including supplementary materials and methods, quantitative analyses, and supporting figures of peptide characterization, bioactivity assays, and *in vivo* evaluations) is available in the online version of this article at https://doi.org/10.26599/NR.2026.94908544.

Data availability

All data needed to support the conclusions in the paper are presented in the manuscript and the Electronic Supplementary Material. Additional data related to this paper may be requested from the corresponding author upon request.

Acknowledgements

This work was supported by the National Natural Science Foundation of China (No. 22088102), the New Cornerstone Science Foundation, and the Natural Science Foundation of Beijing Municipality (No. 2222051). The authors also acknowledge the technical support provided by Core Facility Center at Capital Medical University.

Declaration of competing interest

All the contributing authors report no conflict of interests in this work.

Author contribution statement

X. S.: Investigation, writing – original draft. Z. Y. W.: Data curation. Y. W.: Visualization. Y. X. S. : Validation. X.-W. G.: Methodology. S. M. Y.: Methodology. J. Q. S.: Methodology. K. F.: Methodology, writing – review & editing. B. C.: Writing – review & editing. N. X.: Conceptualization, project administration, supervision, writing – review & editing. C.-H. T.: Writing – review & editing. L.-Z. W.: Supervision, writing – review & editing.

Informed consent

Not applicable.

Ethics statement

The animal experiments were carried out following the guidelines of the Animal Care Unit at Capital Medical University and were approved by the Animal Ethics Committee of Capital Medical University (Ethical code: AEEI2025550).

Use of AI statement

None.

References

[1] Sheehan, F.; Sementa, D.; Jain, A.; Kumar, M.; Tayarani-Najjaran, M.; Kroiss, D.; Ulijn, R. V. Peptide-based supramolecular systems chemistry. *Chem. Rev.* **2021**, *121*, 13869–13914.

[2] Li, Y. T.; Lu, H. F.; Lu, L. H.; Wang, H. M. Engineering peptide self-assembly: Modulating noncovalent interactions for biomedical applications. *Acc. Mater. Res.* **2025**, *6*, 447–461.

[3] Aida, T.; Meijer, E. W.; Stupp, S. I. Functional supramolecular polymers. *Science* **2012**, *335*, 813–817.

[4] Zhao, F. Y.; Liu, M. Z.; Guo, H.; Wang, Y.; Zhang, Y. Q.; He, M. X.; Cai, Z. Y. Stimuli-responsive hydrogels based on protein/peptide and their sensing applications. *Prog. Mater. Sci.* **2025**, *148*, 101355.

[5] Fu, K.; Wu, H. G.; Su, Z. Q. Self-assembling peptide-based hydrogels: Fabrication, properties, and applications. *Biotechnol. Adv.* **2021**, *49*, 107752.

[6] Hur, Y. M.; Min, K. I. Harnessing amino acid modularity for programmable function in covalent peptide assemblies. *Adv. Mater.* **2025**, *37*, 2419941.

[7] Dou, X. Q.; Feng, C. L. Amino acids and peptide-based supramolecular hydrogels for three-dimensional cell culture. *Adv. Mater.* **2017**, *29*, 1604062.

[8] Guan, T.; Li, J. Y.; Chen, C. Y.; Liu, Y. Self-assembling peptide-based hydrogels for wound tissue repair. *Adv. Sci.* **2022**, *9*, 2104165.

[9] Liu, H. Y.; Song, Z. L.; Zhang, Y.; Wu, B. H.; Chen, D. H.; Zhou, Z. A.; Zhang, H. Y.; Li, S. S.; Feng, X. P.; Huang, J. et al. De novo design of self-assembling peptides with antimicrobial activity guided by deep learning. *Nat. Mater.* **2025**, *24*, 1295–1306.

[10] Liu, Y. C.; Gong, H. N.; Wang, Z. W.; Yuan, C. Q.; Lu, J. R.; Yan, X. H. Treatment of superbug infection through a membrane-disruption and immune-regulation cascade effect based on supramolecular peptide hydrogels. *Adv. Funct. Mater.* **2023**, *33*, 2305726.

[11] Lu, P. L.; Ruan, D. X.; Huang, M. Q.; Tian, M.; Zhu, K. S.; Gan, Z. Q.; Xiao, Z. C. Harnessing the potential of hydrogels for advanced therapeutic applications: Current achievements and future directions. *Signal Transduct. Target. Ther.* **2024**, *9*, 166.

[12] Hao, Y. S.; Li, H.; Guo, J. J.; Wang, D.; Zhang, J. M.; Liu, J. J.; Yang, C. H.; Zhang, Y. M.; Li, G. L.; Liu, J. F. Bio-inspired antioxidant heparin-mimetic peptide hydrogel for radiation-induced skin injury repair. *Adv. Healthc. Mater.* **2023**, *12*, 2203387.

[13] Li, L. L.; Qiao, Z. Y.; Wang, L.; Wang, H. Programmable construction of peptide-based materials in living subjects: From modular design and morphological control to theranostics. *Adv. Mater.* **2019**, *31*, 1804971.

[14] Coulter, S. M.; Pentlavalli, S.; An, Y. M.; Vora, L. K.; Cross, E. R.; Moore, J. V.; Sun, H.; Schweins, R.; McCarthy, H. O.; Laverty, G. *In situ* forming, enzyme-responsive peptoid-peptide hydrogels: An advanced long-acting injectable drug delivery system. *J. Am. Chem. Soc.* **2024**, *146*, 21401–21416.

[15] Liang, Y. P.; He, J. H.; Guo, B. L. Functional hydrogels as wound dressing to enhance wound healing. *ACS Nano* **2021**, *15*, 12687–12722.

[16] Xuan, Q. Z.; Jiang, F.; Dong, H.; Zhang, W. X.; Zhang, F. Y.; Ma, T. H.; Zhuang, J. F.; Yu, J. L.; Wang, Y. B.; Shen, H. et al. Bioinspired intrinsic versatile hydrogel fabricated by amyloidal toxin simulant-based nanofibrous assemblies for accelerated diabetic wound healing. *Adv. Funct. Mater.* **2021**, *31*, 2106705.

[17] Zhang, Y.; Wang, Y. F.; Guan, Y.; Zhang, Y. J. Peptide-enhanced tough, resilient and adhesive eutectogels for highly reliable strain/pressure sensing under extreme conditions. *Nat. Commun.* **2022**, *13*, 6671.

[18] Chen, Z. J.; Wang, L. L.; Guo, C. J.; Qiu, M. L.; Cheng, L.; Chen, K. Z.; Qi, J.; Deng, L. F.; He, C.; Li, X. M. et al. Vascularized polypeptide hydrogel modulates macrophage polarization for wound healing. *Acta Biomater.* **2023**, *155*, 218–234.

[19] Liu, H.; Wei, X. M.; Peng, H. G.; Yang, Y.; Hu, Z.; Rao, Y. F.; Wang, Z. F.; Dou, J. X.; Huang, X. N.; Hu, Q. W. et al. LysSYL-loaded Ph-switchable self-assembling peptide hydrogels promote methicillin-resistant *Staphylococcus aureus* elimination and wound healing. *Adv. Mater.* **2024**, *36*, 2412154

[20] Wang, H.; Mu, G. N.; Cai, X. Y.; Zhang, X. G.; Mao, R. Q.; Jia, H. X.; Luo, H. J.; Liu, J. F.; Zhao, C. C.; Wang, Z. Y. et al. Glucopeptide superstructure hydrogel promotes surgical wound healing following neoadjuvant radiotherapy by producing NO and anticellular senescence. *Adv. Healthc. Mater.* **2024**, *13*, 2400406.

[21] Zhao, C. K.; Li, X.; Han, X. W.; Li, Z. L.; Bian, S. Q.; Zeng, W. N.; Ding, M. M.; Liang, J.; Jiang, Q.; Zhou, Z. K. et al. Molecular co-assembled strategy tuning protein conformation for cartilage regeneration. *Nat. Commun.* **2024**, *15*, 1488.

[22] Farsheed, A. C.; Thomas, A. J.; Pogostin, B. H.; Hartgerink, J. D. 3D

printing of self-assembling nanofibrous multidomain peptide hydrogels. *Adv. Mater.* **2023**, *35*, 2210378.

[23] Farsheed, A. C.; Zevallos-Delgado, C.; Yu, L. T.; Saeidifard, S.; Swain, J. W. R.; Makhoul, J. T.; Thomas, A. J.; Cole, C. C.; Garcia Huitron, E.; Grande-Allen, K. J. et al. Tunable macroscopic alignment of self-assembling peptide nanofibers. *ACS Nano* **2024**, *18*, 12477–12488.

[24] Sangji, M. H.; Lee, S. R.; Sai, H.; Weigand, S.; Palmer, L. C.; Stupp, S. I. Self-sorting *vs* coassembly in peptide amphiphile supramolecular nanostructures. *ACS Nano* **2024**, *18*, 15878–15887.

[25] Clarke, D. E.; Parmenter, C. D. J.; Scherman, O. A. Tunable pentapeptide self-assembled *β*-sheet hydrogels. *Angew. Chem. Int. Ed.* **2018**, *57*, 7709–7713.

[26] Wang, J. H.; Chen, X. Y.; Zhao, Y.; Yang, Y. M.; Wang, W. 10.1021/acsnano.9b05608J.; Wu, C.; Yang, B. Z.; Zhang, Z. T.; Zhang, L. S.; Liu, Y. et al. pH-switchable antimicrobial nanofiber networks of hydrogel eradicate biofilm and rescue stalled healing in chronic wounds. *ACS Nano* **2019**, *13*, 11686–11697.

[27] Carlini, A. S.; Choi, W.; McCallum, N. C.; Gianneschi, N. C. pH-responsive charge-conversion progelator peptides. *Adv. Funct. Mater.* **2021**, *31*, 2007733.

[28] Clover, T. M.; O'Neill, C. L.; Appavu, R.; Lokhande, G.; Gaharwar, A. K.; Posey, A. E.; White, M. A.; Rudra, J. S. Self-assembly of block heterochiral peptides into helical tapes. *J. Am. Chem. Soc.* **2020**, *142*, 19809–19813.

[29] Wu, B. H.; Zhao, S.; Yang, X. J.; Zhou, L. C.; Ma, Y.; Zhang, H. Y.; Li, W. B.; Wang, H. M. Biomimetic heterodimerization of tetrapeptides to generate liquid crystalline hydrogel in a two-component system. *ACS Nano* **2022**, *16*, 4126–4138.

[30] Liu, R. J.; Dong, X.; Seroski, D. T.; Soto Morales, B.; Wong, K. M.; Robang, A. S.; Melgar, L.; Angelini, T. E.; Paravastu, A. K.; Hall, C. K. et al. Side-chain chemistry governs hierarchical order of charge-complementary β-sheet peptide coassemblies. *Angew. Chem., Int. Ed.* **2023**, *62*, e202314531.

[31] Xiang, Y. X.; Mao, H.; Tong, S. C.; Liu, C.; Yan, R.; Zhao, L.; Zhu, L. Y.; Bao, C. Y. A facile and versatile approach to construct photoactivated peptide hydrogels by regulating electrostatic repulsion. *ACS Nano* **2023**, *17*, 5536–5547.

[32] Arad, E.; Levi, T.; Yosefi, G.; Kass, I.; Cohen-Erez, I.; Azoulay, Z.; Bitton, R.; Jelinek, R.; Rapaport, H. A matter of charge: Electrostatically tuned coassembly of amphiphilic peptides. *Small* **2024**, *20*, 2404324.

[33] Li, X.; Bian, S. Q.; Zhao, M. D.; Han, X. W.; Liang, J.; Wang, K. F.; Jiang, Q.; Sun, Y.; Fan, Y. J.; Zhang, X. D. Stimuli-responsive biphenyl-tripeptide supramolecular hydrogels as biomimetic extracellular matrix scaffolds for cartilage tissue engineering. *Acta Biomater.* **2021**, *131*, 128–137.

[34] Liu, M. H.; Wang, Z. Y.; Feng, D. D.; Shang, Y. N.; Li, X. X.; Liu, J. F.; Li, C.; Yang, Z. M. An insulin-inspired supramolecular hydrogel for prevention of type 1 diabetes. *Adv. Sci.* **2021**, *8*, 2003599.

[35] Jia, H. X.; Lin, J.; Wang, D. Y.; Lv, X.; Wang, Q.; Wang, Z. Y.; Liu, J. J.; Yang, L. J.; Liu, J. F. A Mn^{2+}-assisted nanofiber-hydrogel adjuvant for simultaneous enhancement of humoral and cellular immune responses. *Adv. Funct. Mater.* **2024**, *34*, 2315442.

[36] Li, G. Y.; Deng, H. R.; Xu, W. Y.; Chen, W. W.; Lai, Z. H.; Zhu, Y. J.; Zhang, L. C.; Shao, C. X.; Shan, A. S. Combating antibiotic-resistant bacterial infection using coassembled dimeric antimicrobial peptide-based nanofibers. *ACS Nano* **2025**, *19*, 3155–3171.

[37] Yu, Z. L.; Erbas, A.; Tantakitti, F.; Palmer, L. C.; Jackman, J. A.; de la Cruz, M. O.; Cho, N. J.; Stupp, S. I. Co-assembly of peptide amphiphiles and lipids into supramolecular nanostructures driven by anion-π interactions. *J. Am. Chem. Soc.* **2017**, *139*, 7823–7830.

[38] Nambiar, M.; Wang, L. S.; Rotello, V.; Chmielewski, J. Reversible hierarchical assembly of trimeric coiled-coil peptides into banded nano-and microstructures. *J. Am. Chem. Soc.* **2018**, *140*, 13028–13033.

[39] Sun, S.; Liang, H. W.; Wang, H.; Zou, Q. M. Light-triggered self-assembly of peptide nanoparticles into nanofibers in living cells through molecular conformation changes and H-bond interactions. *ACS Nano* **2022**, *16*, 18978–18989.

[40] Silk, M. R.; Mohanty, B.; Sampson, J. B.; Scanlon, M. J.; Thompson, P. E.; Chalmers, D. K. Controlled construction of cyclic D/L peptide nanorods. *Angew. Chem., Int. Ed.* **2019**, *58*, 596–601.

[41] Zottig, X.; Al-Halifa, S.; Côté-Cyr, M.; Calzas, C.; Le Goffic, R.; Chevalier, C.; Archambault, D.; Bourgault, S. Self-assembled peptide nanorod vaccine confers protection against influenza A virus. *Biomaterials* **2021**, *269*, 120672.

[42] Wu, Y. Y.; Li, Y. M.; Yan, N.; Huang, J. Q.; Li, X. Y.; Zhang, K. Y.; Lu, Z. M.; Qiu, Z. W.; Cheng, H. Nuclear-targeted chimeric peptide nanorods to amplify innate anti-tumor immunity through localized DNA damage and STING activation. *J. Control. Release* **2024**, *369*, 531–544.

[43] Sinha, N. J.; Langenstein, M. G.; Pochan, D. J.; Kloxin, C. J.; Saven, J. G. Peptide design and self-assembly into targeted nanostructure and functional materials. *Chem. Rev.* **2021**, *121*, 13915–13935.

[44] Chen, X.; Xia, C.; Guo, P.; Wang, C. R.; Zuo, X. B.; Jiang, Y. B.; Jiang, T. Preserving structurally labile peptide nanosheets after molecular functionalization of the self-assembling peptides. *Angew. Chem., Int. Ed.* **2024**, *63*, e202315296.

[45] He, Y. M.; Zhu, X. H.; Wang, L.; Zhang, Y.; Bai, C.; Wu, D. D. Multi-responsive peptide-based ultrathin nanosheets prepared by a horizontal monolayer assembly. *Angew. Chem., Int. Ed.* **2024**, *63*, e202405765.

[46] Liu, J.; Wu, W. W.; Peng, F.; Gong, D. Y.; Kang, Y.; Zhang, Y. J.; Liu, C. Y.; Li, Y. C.; Zhao, G. Y.; Qiu, F. et al. Size control of ropivacaine nano/micro-particles by soft-coating with peptide nanosheets for long-acting analgesia. *Theranostics* **2024**, *14*, 2637–2655.

[47] Novelli, F.; Vilela, M.; Pazó, A.; Amorín, M.; Granja, J. R. Molecular plumbing to bend self-assembling peptide nanotubes. *Angew. Chem., Int. Ed.* **2021**, *60*, 18838–18844.

[48] Zhao, Y. R.; Hu, X. Z.; Zhang, L. M.; Wang, D.; King, S. M.; Rogers, S. E.; Wang, J. Q.; Lu, J. R.; Xu, H. Monolayer wall nanotubes self-assembled from short peptide bolaamphiphiles. *J. Colloid Interface Sci.* **2021**, *583*, 553–562.

[49] Wang, Y. H.; Rencus-Lazar, S.; Zhou, H. R.; Yin, Y. Y.; Jiang, X. M.; Cai, K. Y.; Gazit, E.; Ji, W. Bioinspired amino acid based materials in bionanotechnology: From minimalistic building blocks and assembly mechanism to applications. *ACS Nano* **2024**, *18*, 1257–1288.

[50] Ma, X. Y.; Zhao, Y. R.; Jiang, X. F.; Fan, M. C.; He, C. Y.; Qi, H.; Wang, Y.; Wang, D.; Ke, Y. B.; Xu, H. et al. Controlled assembly and disassembly of higher-order peptide nanotubes. *ACS Appl. Mater. Interfaces* **2024**, *16*, 9787–9798.

[51] Li, X. Y.; Gong, J. P. Design principles for strong and tough hydrogels. *Nat. Rev. Mater.* **2024**, *9*, 380–398.

[52] Kopyeva, I.; Brady, R. P.; DeForest, C. A. Light-based fabrication and 4D customization of hydrogel biomaterials. *Nat. Rev. Bioeng.* **2025**, *3*, 159–180.

[53] Dong, H. L.; Wang, M. S.; Fan, S. H.; Wu, C. L.; Zhang, C. H.; Wu, X.; Xue, B.; Cao, Y.; Deng, J. J.; Yuan, D. et al. Redox-regulated conformational change of disulfide-rich assembling peptides. *Angew. Chem., Int. Ed.* **2022**, *61*, e202212829.

[54] Huang, W. J.; Dong, H. L.; Yan, Q. P.; Deng, T. F.; Li, X. X.; Zhao, Z.; Li, Z. H.; Wang, M. S.; Zhang, C. H.; Kong, B. et al. Disulfide-rich self-assembling peptides based on aromatic amino acid. *Small* **2025**, *21*, 2407464.

[55] Qiao, Y. S.; Liu, X. Z.; Zhou, X. C.; Zhang, H. B.; Zhang, W.; Xiao, W.; Pan, G. Q.; Cui, W. G.; Santos, H. A.; Shi, Q. Gelatin templated polypeptide co-cross-linked hydrogel for bone regeneration. *Adv. Healthc. Mater.* **2020**, *9*, 1901239.

[56] Huang, J. J.; Yang, R.; Jiao, J.; Li, Z.; Wang, P. H.; Liu, Y.; Li, S. C.;

Chen, C. W.; Li, Z.; Qu, G. W. et al. A click chemistry-mediated all-peptide cell printing hydrogel platform for diabetic wound healing. *Nat. Commun.* **2023**, *14*, 7856.

[57] Xiang, Y. X.; Liu, C.; Ma, S. N.; Wang, X. T.; Zhu, L. Y.; Bao, C. Y. Stimuli-responsive peptide self-assembly to construct hydrogels with actuation and shape memory behaviors. *Adv. Funct. Mater.* **2023**, *33*, 2300416.

[58] Liu, P. Y.; Zhang, Y.; Guan, Y.; Zhang, Y. J. Peptide-crosslinked, highly entangled hydrogels with excellent mechanical properties but ultra-low solid content. *Adv. Mater.* **2023**, *35*, 2210021.

[59] Zheng, Y. F.; Zhang, S.; Yuan, Y.; Li, C. Hierarchical engineering of amphiphilic peptides nanofibrous crosslinkers toward mechanically robust, functionally customable, and sustainable supramolecular hydrogels. *Adv. Mater.* **2025**, *37*, 2503324.

[60] Teng, R. X.; Yang, Y. Y.; Zhang, Z.; Yang, K. X.; Sun, M.; Li, C.; Fan, Z.; Du, J. Z. *In situ* enzyme-induced self-assembly of antimicrobial-antioxidative peptides to promote wound healing. *Adv. Funct. Mater.* **2023**, *33*, 2214454.

[61] Yu, S. H.; Ye, Z.; Roy, R.; Sonani, R. R.; Pramudya, I.; Xian, S. J.; Xiang, Y. H.; Liu, G. Q.; Flores, B.; Nativ-Roth, E. et al. Glucose-triggered gelation of supramolecular peptide nanocoils with glucose-binding motifs. *Adv. Mater.* **2024**, *36*, 2311498.

[62] Xue, B.; Bashir, Z.; Guo, Y. C.; Yu, W. T.; Sun, W. X.; Li, Y. R.; Zhang, Y. Y.; Qin, M.; Wang, W.; Cao, Y. Strong, tough, rapid-recovery, and fatigue-resistant hydrogels made of picot peptide fibres. *Nat. Commun.* **2023**, *14*, 2583.

[63] Guan, T.; Chen, Z. W.; Wang, X.; Gao, S. S.; Lu, X. Y.; Li, Y.; Wang, Z. C.; Zhang, S. H.; Guo, Y. C.; Guo, M. Y. et al. Harnessing Mn^{2+} ions and antitumor peptides: A robust hydrogel for enhanced tumor immunotherapy. *J. Am. Chem. Soc.* **2025**, *147*, 6523–6535.

[64] Zhao, J. Y.; Li, C.; Gao, X. W.; Feng, K.; Liu, H.; He, S. J.; Zhao, W. H.; Yang, S. M.; Shao, J. Q.; Ye, L. et al. Quick photofabrication of functional nanospheres from *de novo* designed peptides for NIR fluorescence and MR imaging. *Nano Res.* **2023**, *16*, 4029–4038.

[65] He, S. J.; Shu, X.; Wang, Z. Y.; Gao, X. W.; Feng, K.; Yang, S. M.; Shao, J. Q.; Xie, N. Photofabrication of fluorescent nanospheres from *de novo* designed peptides, and their enzyme-responsive dissociation in living cells. *Mater. Adv.* **2024**, *5*, 2888–2897.

[66] Jia, Y. P.; Zhang, Y.; Zhan, W. J.; Wang, Y.; Sun, X. B.; Zhang, Y.; Liu, X. Y.; Han, B.; Bai, Y.; Shen, L. et al. Sustained release of neuroprotective drugs curcumin and edaravone from supramolecular hydrogel for ischemic stroke treatment. *Adv. Funct. Mater.* **2023**, *33*, 2303930.

[67] Yang, T. J.; Xue, T. R.; Mao, J. N.; Chen, Y. Y.; Tian, H. D.; Bartolome, A.; Xia, H. W.; Yao, X. D.; Kumar, C. V.; Cheng, J. J. et al. Tailoring synthetic polypeptide design for directed fibril superstructure formation and enhanced hydrogel properties. *J. Am. Chem. Soc.* **2024**, *146*, 5823–5833.

[68] Zhang, Y.; Liu, H. Y.; Zhang, W. Q.; Ding, Y. H.; Zhang, S. Y.; Huang, X. W.; Chen, J. L.; Yang, Z. M.; Lin, F. Injectable iodine-containing peptide hydrogel for treatment of MRSA infection. *Bioact. Mater.* **2025**, *47*, 198–208.

[69] Schnaider, L.; Brahmachari, S.; Schmidt, N. W.; Mensa, B.; Shaham-Niv, S.; Bychenko, D.; Adler-Abramovich, L.; Shimon, L. J. W.; Kolusheva, S.; DeGrado, W. F. et al. Self-assembling dipeptide antibacterial nanostructures with membrane disrupting activity. *Nat. Commun.* **2017**, *8*, 1365.

[70] Abbas, M.; Ovais, M.; Atiq, A.; Ansari, T. M.; Xing, R. R.; Spruijt, E.; Yan, X. H. Tailoring supramolecular short peptide nanomaterials for antibacterial applications. *Coord. Chem. Rev.* **2022**, *460*, 214481.

[71] Doolan, J. A.; Williams, G. T.; Hilton, K. L. F.; Chaudhari, R.; Fossey, J. S.; Goult, B. T.; Hiscock, J. R. Advancements in antimicrobial nanoscale materials and self-assembling systems. *Chem. Soc. Rev.* **2022**, *51*, 8696–8755.

[72] Chen, B.; Thurber, K. R.; Shewmaker, F.; Wickner, R. B.; Tycko, R. Measurement of amyloid fibril mass-per-length by tilted-beam transmission electron microscopy. *Proc. Natl. Acad. Sci. USA* **2009**, *106*, 14339–14344.

[73] Allam, T.; Balderston, D. E.; Chahal, M. K.; Hilton, K. L. F.; Hind, C. K.; Keers, O. B.; Lilley, R. J.; Manwani, C.; Overton, A.; Popoola, P. I. A. et al. Tools to enable the study and translation of supramolecular amphiphiles. *Chem. Soc. Rev.* **2023**, *52*, 6892–6917.

[74] Chen, S.; Li, Z. H.; Zhang, C. H.; Wu, X.; Wang, W. J.; Huang, Q. J.; Chen, W. Y.; Shi, J. F.; Yuan, D. Cation-π interaction trigger supramolecular hydrogelation of peptide amphiphiles. *Small* **2023**, *19*, 2301063.

[75] Pan, X. H.; Li, R.; Li, W. Y.; Sun, W.; Yan, Y. Y.; Xiang, X. C.; Fang, J. H.; Liao, Y. G.; Xie, C.; Wang, X. Z. et al. Silk fibroin hydrogel adhesive enables sealed-tight reconstruction of meniscus tears. *Nat. Commun.* **2024**, *15*, 2651.

[76] Chakraborty, P.; Tang, Y. M.; Yamamoto, T.; Yao, Y. F.; Guterman, T.; Zilberzwige-Tal, S.; Adadi, N.; Ji, W.; Dvir, T.; Ramamoorthy, A. et al. Unusual two-step assembly of a minimalistic dipeptide-based functional hypergelator. *Adv. Mater.* **2020**, *32*, 1906043.

[77] Han, A. L.; Han, P. J.; Xu, B. L.; Li, Y. H.; Wu, Q. Y.; Li, S. S.; Sun, Y.; Tong, Y. G.; Liu, H. Y.; Fan, H. H. Rational design of copper-based metallic nano-antibiotic against drug-resistant bacteria infection. *Small* **2025**, *21*, e07067.

[78] Xu, Z. J.; Han, S. Y.; Gu, Z. P.; Wu, J. Advances and impact of antioxidant hydrogel in chronic wound healing. *Adv. Healthc. Mater.* **2020**, *9*, 1901502.

[79] Liu, D. N.; Wang, Y. Q.; Sun, Q.; Mei, D.; Wang, X. L.; Su, Y.; Zhang, J.; Huo, R.; Tian, Y.; Liu, S. Y. et al. Iron and siRNA co-encapsulated ferritin nanocages induce ferroptosis synergistically for cancer therapy. *Acta Pharm. Sin. B* **2025**, *15*, 526–541.

[80] Xu, M.; Liao, J. L.; Li, J. J.; Shi, Y.; Zhang, Z. Y.; Fu, Y. F.; Gu, Z. Z.; Xu, H. Elastic nanoparticle-reinforced, conductive structural color hydrogel with super stretchability, self-adhesion, self-healing as electrical/optical dual-responsive visual electronic skins. *Exploration* **2025**, *5*, 270008.

[81] Wei, L. Q.; Liu, X.; Li, Y. Q.; Han, Y.; Ren, Y. P.; Zou, T. S.; Yu, P. C.; Chen, Y. N.; Zhang, B.; Wang, Z. X. et al. Multifunctional PHC bandage for accelerated wound healing in movable parts. *Exploration* **2025**, *5*, 20230176.

[82] Han, A. L.; Liu, C.; Wu, Q. Y.; Gong, Z. Y.; Liu, M. Q.; Xu, B. L.; Su, X. External physical field-responsive nanocomposite hydrogels for wound healing applications. *Adv. Nanocompos.* **2025**, *2*, 32–58.